Earth and Planetary Science Letters 566 (2021) 116947

Contents lists available at ScienceDirect

Earth and Planetary Science Letters

www.elsevier.com/locate/epsl

Mercury and sulfur isotopic evidence for the linkages between the ca. 510 Ma Kalkarindji large igneous province and trilobite crisis

Ze-Rui Ray Liu [a,b], Mei-Fu Zhou [a,b,*], Wei Terry Chen [c], Anthony E. Williams-Jones [d], Xiang-Dong Li [e], Run-Sheng Yin [c], Hugh O'Brien [f], Yann Lahaye [f]

[a] School of Earth Resources, China University of Geosciences, Wuhan 430074, China
[b] Department of Earth Sciences, The University of Hong Kong, Pokfulam Road, Hong Kong, China
[c] State Key Laboratory of Ore Deposit Geochemistry, Institute of Geochemistry, Chinese Academy of Sciences, Guiyang 550081, China
[d] Department of Earth and Planetary Sciences, McGill University, 3450 University Street, Montreal, QC H3A 0E8, Canada
[e] Department of Civil and Environmental Engineering, The Hong Kong Polytechnic University, Hung Hom, Kowloon, Hong Kong, China
[f] Geological Survey of Finland, 02150 Espoo, Finland

ARTICLE INFO

Article history:
Received 28 July 2020
Received in revised form 30 March 2021
Accepted 9 April 2021
Available online 27 April 2021
Editor: F. Moynier

Keywords:
Hg-S-C isotopes
pyrite
Cambrian Series 2
Miaolingian
calcareous shales
Nanhua Basin

ABSTRACT

The first major mass extinction of trilobites occurred at the transition from Cambrian Series 2 (CS_2) to Miaolingian (M) and coincided with a large marine transgression and volcanic eruptions of a large igneous province (LIP). Understanding the causal links between these events is important in deciphering environmental changes and life evolution at that time. This paper presents S-Hg-C isotopic and Fe speciation data for calcareous shales from the CS_2-M Yangliugang Formation in the Dongjin section, South China. In the lower part of this section (Interval I), calcareous shales have limited S isotopic differences between carbonate-associated sulfates ($\delta^{34}S_{CAS}$) and pyrites ($\delta^{34}S_{Py}$) with $\Delta^{34}S$ values from –4.2‰ to +8.3‰; they also have high Fe_{HR}/Fe_T ratios from 0.5 to 0.66, that are indicative of a low SO_4^{2-} content in anoxic seawater. Calcareous shales from Interval I display at least two Hg/TOC peaks (up to 207 ppb/wt%), coincident with volcanic eruptions associated with the ca. 510 Ma Kalkarindji LIP in Australia. In the middle part of the Dongjin section (Interval II), calcareous shales display negative excursions of $\Delta^{199}Hg$ values, $\delta^{34}S_{Py}$ values and Fe_{HR}/Fe_T ratios, which were likely led by a large terrestrial input into a marginal basin from where Interval II deposited. Calcareous shales in the upper part of the section (Interval III) contain pyrite framboids with a mean diameter of <4 μm and high ratios of Fe_{HR}/Fe_T (>0.82) and Fe_{Py}/Fe_{HR} (>0.78), indicating an euxinic depositional environment. They also record negative excursions in $\delta^{13}C$ and $\delta^{202}Hg$ (with low values down to –3.05‰ and –1.68‰, respectively), providing evidence for ocean upwelling. The negative shift of $\delta^{13}C$ values in the Dongjin section was temporally comparable to the C isotope excursions that coincided with the Redlichiid-Olenellid Extinction Carbon Isotope Excursion (ROECE). We conclude that volcanic eruptions of the ca. 510 Ma Kalkarindji LIP enhanced the continental erosion rate, leading to a high terrestrial SO_4^{2-} input and an accumulation of H_2S in deep marginal basins at the end of CS_2. The subsequent ocean upwelling (>506 Ma) brought anoxic/euxinic seawaters into the continental shelf, contributing to the mass extinction of Redlichiid and Olenellid.

1. Introduction

The Cambrian was an important period in Earth's history marked by a sudden appearance of most major animal phyla (Darroch et al., 2018; Paterson et al., 2019). Trilobites, one of the earliest known groups of arthropods, appeared at the beginning of Cambrian Series 2 (CS_2; 521–506 Ma) and diversified rapidly with oceanic oxidation (Karlstrom et al., 2020; Paterson et al., 2019). The Redlichiid and Olebellid, two of three major trilobite taxa in CS_2 (Paradoxidids being the other taxon), suddenly disappeared at the CS_2-Miaolingian (CS_2-M) transition, roughly coeval with a globally recognizable negative carbon isotope excursion (ROECE) (Lin et al., 2019; Sundberg et al., 2020). Eruptions of flood basalts in the ca. 510 Ma Kalkarindji large igneous province (LIP) (Australia) (Fig. 1a) have long been regarded as an important trigger for this biotic crisis, because they were coincident with the trilobite extinction and might have induced ocean anoxia at the CS_2-M transition (Faggetter et al., 2019; Hough et al., 2006; Jourdan et al., 2014; Zhang et al., 2015). Recent chronostratigraphic studies, how-

* Corresponding author.
E-mail address: mfzhou@hku.hk (M.-F. Zhou).

https://doi.org/10.1016/j.epsl.2021.116947
0012-821X/

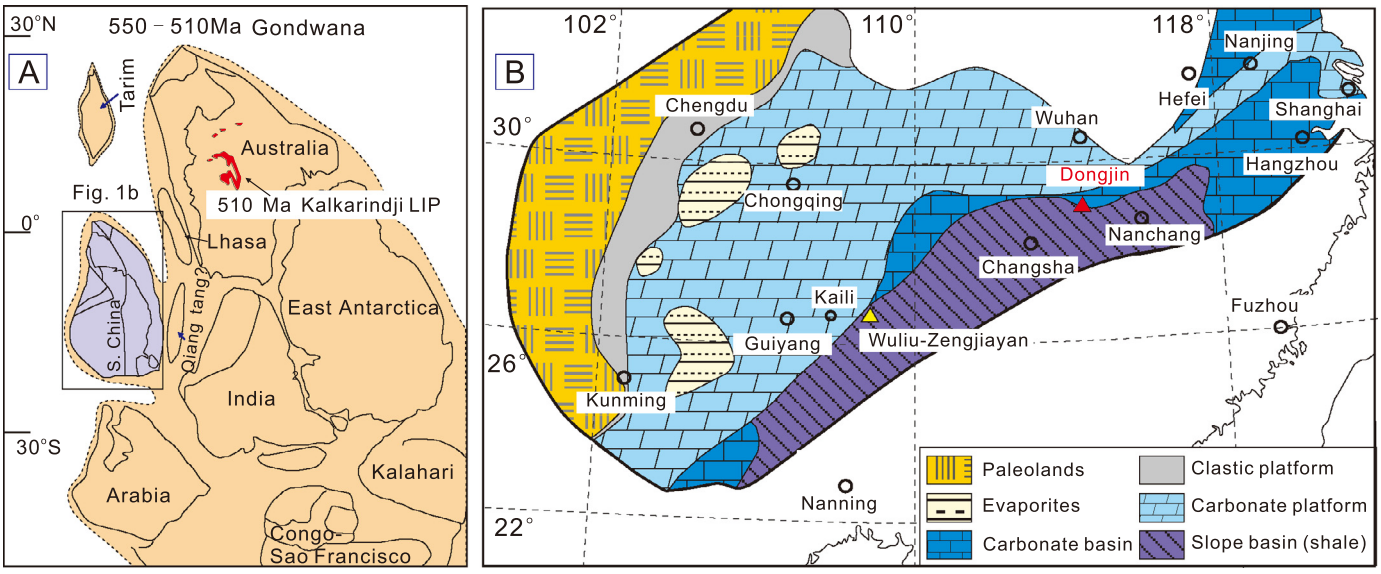

Fig. 1. (A) Geologic setting of the Nanhua Basin, South China (A) global paleogeography of the 550 – 510 Ma Gondwana, showing the location of South China and the 510 Ma Kalkarindji LIP (adapted from Faggetter et al. (2019)). (B) a simplified paleogeographic map of the Nanhua Basin during the CS_2-M transition, showing the three major facies identified by Zhang et al. (2008) and the locations of the Wuliu-Zengjiayan (yellow triangle) and the Dongjin (red triangle) sections. (For interpretation of the colors in the figure(s), the reader is referred to the web version of this article.)

ever, have advanced the time of extinction from ca. 509 Ma to ca. 506 Ma (Karlstrom et al., 2020), placing doubt on a direct link between the mass extinction and the ca. 510 Ma Kalkarindji LIP.

The sulfur isotopic composition of marine sediments is a sensitive indicator of ocean sulfate concentration and redox state (Canfield and Farquhar, 2009; Fike et al., 2015; Gomes and Hurtgen, 2015; Loyd et al., 2012). Cambrian Series 2 and Miaolingian sediments generally have variable $\delta^{34}S_{sulfate}$ values (0 to >+45‰) recorded in gypsum, calcite, dolomite, and apatite (Hough et al., 2006; Kampschulte and Strauss, 2004; Wotte et al., 2012b), and positive $\delta^{34}S_{Py}$ values (0 to >+30‰) (Guo et al., 2014; Loyd et al., 2012; Wotte et al., 2012b). The low $\Delta^{34}S$ values ($\delta^{34}S_{sulfate} - \delta^{34}S_{Py}$) of CS_2-M sediments suggest that the coeval seawater sulfate concentration was low (<2.0 mM; Loyd et al., 2012). A negative shift in $\delta^{34}S_{Py}$ (about −10‰) occurred before the $\delta^{13}C$ excursion (ROECE) (Guo et al., 2010, 2014) and is recognized globally, e.g., in the Wuliu-Zengjiayan and Jianshan sections, South China, the Genestosa and Cre´menes sections, Spain, and the Carro Rajon section, Mexico (Guo et al., 2014; Loyd et al., 2012; Wotte et al., 2012b). However, owing to the low abundance of pyrite in these sections, systematic S isotopic studies based on the mode of occurrence of pyrite have not been carried out, leading to a poor understanding of the reason for this negative shift of $\delta^{34}S_{Py}$ values prior to the mass extinction.

Mercury (Hg) concentrations, the ratios of Hg to total organic carbon (Hg/TOC ratios), and Hg isotopes have recently been developed as novel proxies for investigating mass extinction, large-scale volcanism, and anoxic oceanic events in Earth's history (e.g., Grasby et al., 2019). Anomalously high Hg concentrations and Hg/TOC ratios have been observed in marine sediments associated with all of the 'big five' Phanerozoic mass extinctions, implying that LIP events may contribute to mass extinctions (Grasby et al., 2019). Extensive Hg emission during LIP events increases the input of Hg to the ocean through (1) directly increasing atmospheric Hg deposition (Grasby et al., 2017; Thibodeau et al., 2016) and (2) inducing large-scale surface weathering that causes enhanced watershed runoff of soil Hg (Grasby et al., 2017; Shen et al., 2019, 2020; Them et al., 2019). Mercury isotopes, especially their mass-independent fractionation (MIF) signature, provide constraints on causes of Hg anomalies from atmospheric deposition or soil erosion (Blum et al., 2014; Grasby et al., 2019; Them et al., 2019). Recently, Hg anomalies have been detected in sediments deposited at or before the CS_2-M boundary in the Great Basin (western USA) (Faggetter et al., 2019). Owing to the lack of systematic Hg isotopic data, however, it is unclear whether these Hg anomalies resulted from volcanic emissions or were due to other causes.

The Nanhua Basin in South China was one of the main depositional sites of marine sediments during the Cambrian (Fig. 1b) (Wang and Li, 2003). The Yangliugang Formation in the eastern part of the Nanhua Basin is a time-equivalent of the Kaili Formation in the Wuliu-Zengjiayan section, a Global Boundary Stratotype Section and Point (GSSP) for the boundary between the CS_2 and the M Series (Zhao et al., 2019). Calcareous shales from the CS_2-M Yangliugang Formation in the Dongjin section (N 29°01′09.9″;E 114°18′13.7″), Jiangxi Province, were deposited in a slope-basin environment (Fig. 1) (Zhang et al., 2008). They are characterized by relatively high abundances of pyrite, calcite, and organic matter (Fig. 2). In this study, calcareous shales from the Dongjin section were systematically analyzed for their S-Hg-C isotopic compositions and Fe speciation. Using these data and previous S-C data from the Wuliu-Zengjiayan section and Hg-S-C from sections in other parts of the world, this paper aims to shed light on the linkages between marine redox state, mass extinction, and the volcanic eruption of LIPs during the later stages of the 'Cambrian explosion'.

2. Geological setting

The Nanhua Basin in the South China Craton was opened after the amalgamation of the Yangtze and Cathaysia Blocks at ca. 820 Ma and closed during the Ordovician-Silurian orogeny (Wang and Li, 2003; Yao and Li, 2016). It is widely accepted that the Nanhua Basin was well-connected to the open ocean from the Cambrian Terreneuvian to the Miaolingian (M) Epoch, based on the similarity of the carbonate carbon isotopic ($\delta^{13}C$) signatures (Guo et al., 2014; Lin et al., 2019) and animal fauna (Hughes, 2016; Lin et al., 2019; Paterson et al., 2019) of South China to those of coeval marginal basins in other cratons. From the paleogeography and stratigraphy of the CS_2-M transition, the Nanhua Basin has been subdivided into clastic platform, carbonate platform, carbonate basin, and slope basin facies (Zhang et al., 2008). The Wuliu-

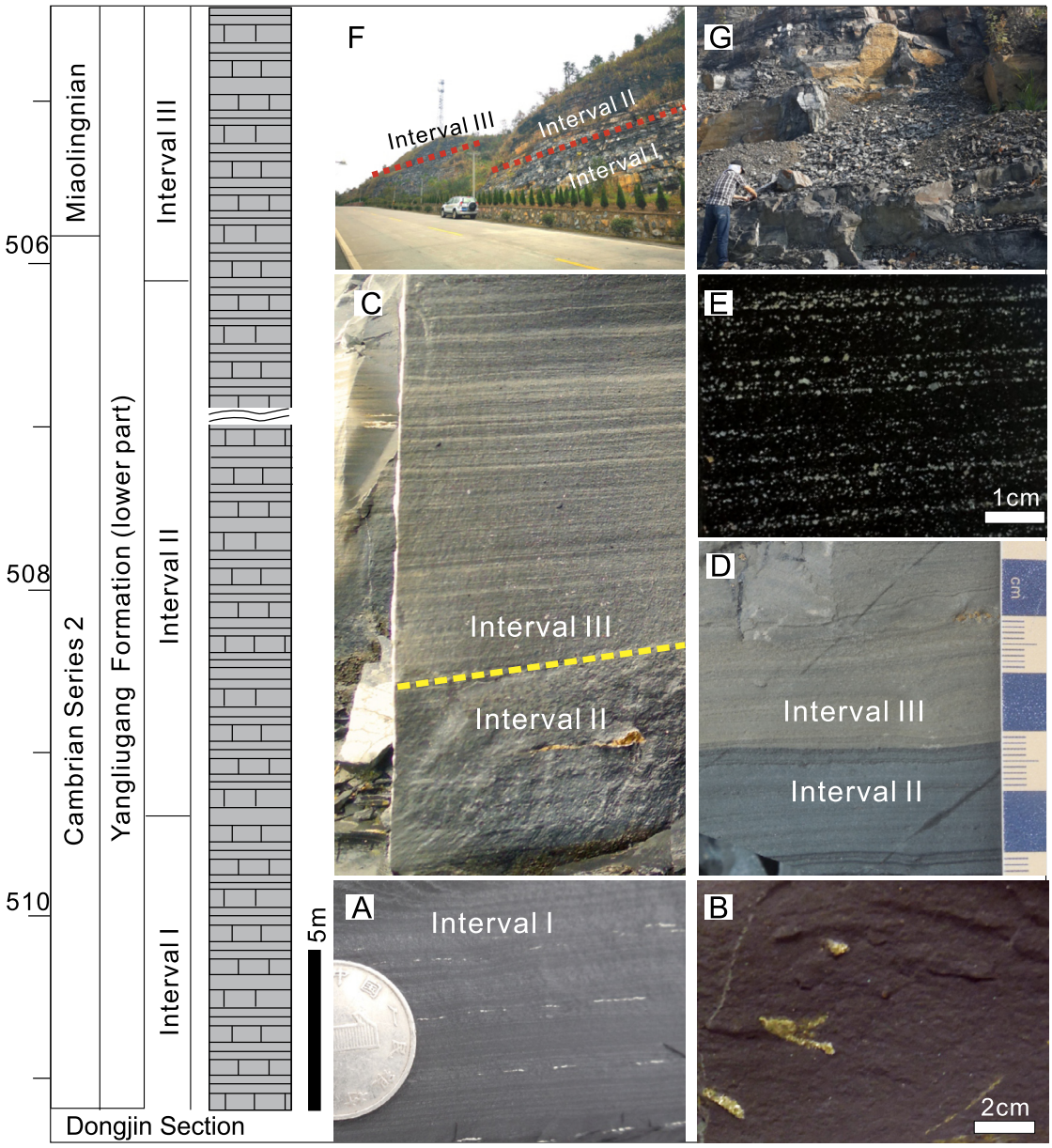

Fig. 2. Stratigraphy and photographs of the Dongjin section, South China. (A) and (B) nodular pyrite aggregates in Interval I; (C) and (D) the boundary between Interval II and Interval III; (E) pyrite layers in calcareous shales from Interval III; (F) and (G) outcrops of the Dongjin section, showing Interval I, II and III.

Zengjiayan section (GSSP) was located in the shale facies of the slope basin in an overall oxic-suboxic depositional environment (Fig. 1b) (Guo et al., 2014). The boundary between the CS_2 and the M Series is marked by the first appearance of *Oryctocephalus Indicus* in the CS_2-M Kaili Formation at ca. 506 Ma (Karlstrom et al., 2020; Sundberg et al., 2020; Zhao et al., 2019), which was coincident with the last appearance datum of Redlichiids in South China (Lin et al., 2019; Sundberg et al., 2020).

A continuous Cambrian succession outcrops in Xiushui county, Jiangxi province, South China (see Supplementary Figure S1 for a regional geological map). The early Cambrian Wangyinpu Formation at the base of this succession, which consists of black shales with cherty interlayers and phosphoric nodules, is correlative to the lower Niutitang Formation in SW China (Liu et al., 2019). This formation is overlain by black shales of the Guanyintang Formation and, in turn, the CS_2-M Yangliugang Formation with thickness of 180 – 310 m. The Yangliugang Formation is dominated by argillaceous limestones, calcareous shales and siliciclastic sedimentary rocks and is overlain by siltstones of the late Cambrian Huayansi and Xiyangshan Formations (Chang et al., 2019; Ju, 1989). Recently, a negative excursion of $\delta^{13}C$ has been recognized in the lower part of the Yangliugang Formation in the Xuancheng section, comparable to the global ROECE excursion at the CS_2-M transition (ca. 506 Ma) (Chang et al., 2019). *Ptychagnoustus gibbus* first appeared in the middle part of the Yangliugang Formation (Ju, 1989; Peng et al., 2012), marking the transition from the Wuliuan Stage to the Drumian Stage at 504.5 Ma (Zhu et al., 2019).

In the Dongjin section, Xiushui county, the lower part of the Yangliugang Formation (ca. 38 m) is well exposed, and the rocks are dominated by organic-rich (ca. 1.0 wt% TOC) argillaceous limestones and calcareous shales (the term calcareous shale is used hereafter to refer to argillaceous limestone and calcareous shale) (Figs. 2 and 3a) that conformably overlie the black shales of the early Cambrian Guanyintang Formation. The calcareous shale successions have been subdivided into three intervals based on the nature and distribution of pyrite in the rocks. Calcareous shales

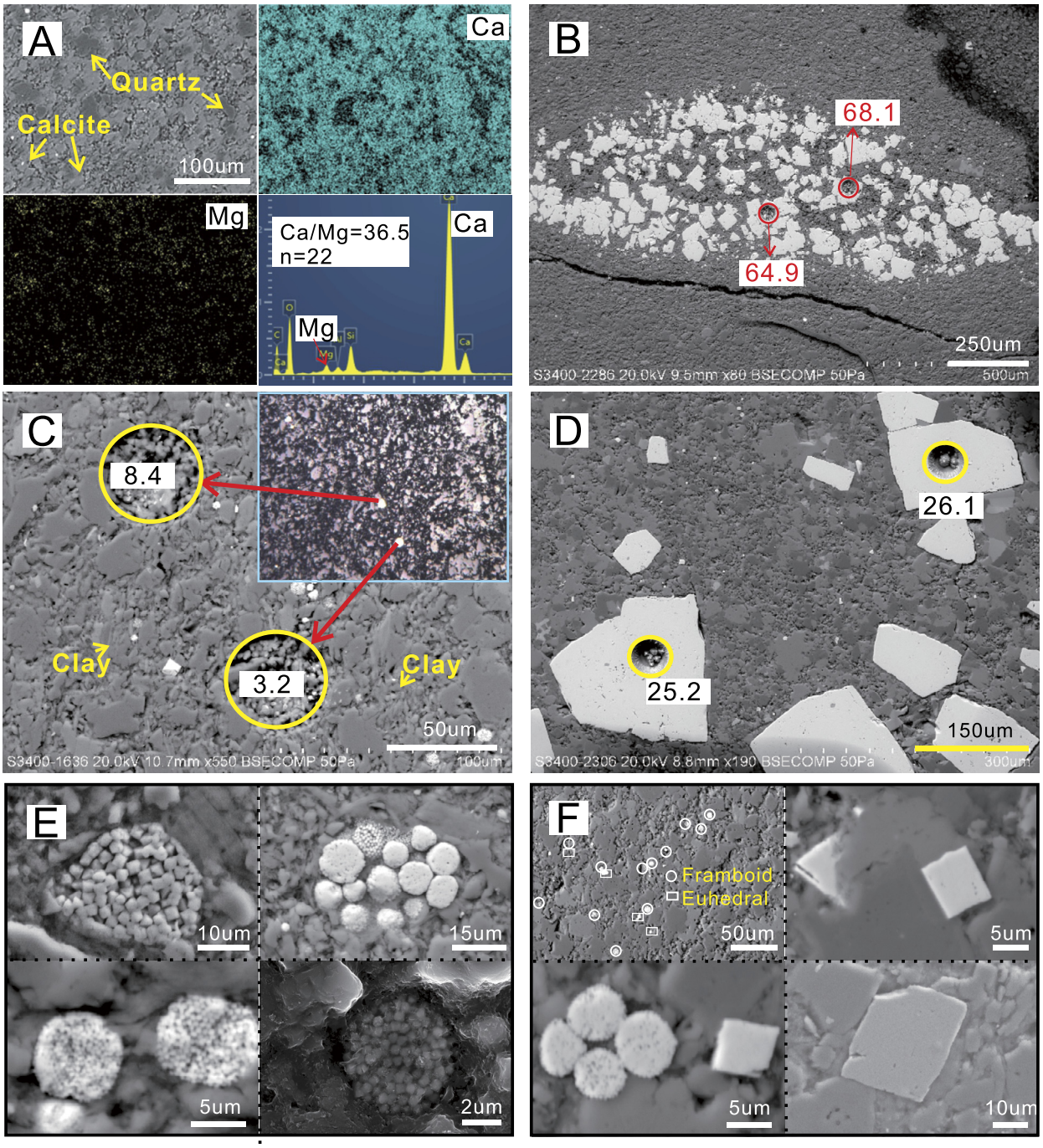

Fig. 3. Morphology and S isotopic composition of different forms of pyrite from the calcareous shales of the Dongjin section, South China. (A) calcites from the calcareous shales; (B) nodular pyrite aggregates in calcareous shales from Interval I with extremely high $\delta^{34}S$ values; (C) disseminated pyrite and corresponding $\delta^{34}S$ values in Interval I; (D) pyrite from calcareous shale of Interval III; (E) pyrite framboids; and (F) occurrences of finely disseminated euhedral pyrite.

from the lower 11 m of the Dongjin section (Interval I) contain layers of pyrite about 2 cm apart and nodular pyrite aggregates (Figs. 2a, b and 3b). In the middle part of this section (Interval II), the abundance of nodular pyrite aggregates decreases rapidly (Figs. 2c and d), and the distance between adjecent pyrite layers increases to > 10 cm. The middle part of Interval II was covered by soil and plant (about 3.5 m in thickness), and was therefore not accessible for sampling. Calcareous shales from Interval III (top 8 m) are rich in pyrite, the content of which increases abruptly to > 5 vol% from field observations and hand specimen estimates (Figs. 2c and e).

3. Sampling and analyses

A total of 38 calcareous shale samples were collected from the Dongjin section with a resolution of one sample per meter for Hg-S-C-Fe-trace element geochemical/isotopic analyses. Fourteen of the samples are from the lower part of Interval II and 5 samples are from the upper part of Interval II. Detailed descriptions of the analytical methods are available in Supplementary Note 1. A brief description of these methods is provided here.

Morphological data for pyrite were collected from polished thin sections, using a Hitachi S-3400N variable pressure scanning elec-

tron microscope (SEM) at the Electron Microscope Unit, the University of Hong Kong. *In-situ* S isotope analyses of pyrite were performed on thin sections (>100 μm in thickness) using a Nu Plasma HR multi-collector inductively coupled plasma mass spectrometer and a Photon Machine Analyte G2 laser microprobe (MC-LA-ICPMS), both at the Geological Survey of Finland in Espoo. Nodular pyrite aggregates in samples from Intervals I and II have $\delta^{34}S_{Py}$ values that are significantly higher than those of disseminated pyrite (Table S1), indicating that the nodular pyrite did not form during sediment deposition or early diagenesis. This pyrite was therefore removed before powdering for bulk rock analysis.

Approximately 500 g of the remaining rock was ground with an agate mortar and pestle for subsequent extraction of H_2S from the disseminated pyrite and extraction of sulfate from the carbonates. Disseminated pyrite was extracted using the chromium reduction method, in which the powders were reacted with 50 ml of 1 M $CrCl_2$ and 20 ml of 10 M HCl in a N_2 atmosphere (Canfield et al., 1986). To eliminate non-CAS compounds and conduct the final extraction of CAS, we used a HCl–$BaCl_2$ procedure similar to that described in Wotte et al. (2012a). Approximately 100 μg $BaSO_4$ (for CAS) or Ag_2S (for pyrite separates) was measured out for analysis of their sulfur isotopic composition using a Thermo Finnigan Delta Plus mass spectrometer connected to an Elemental Analyzer. Carbon and oxygen isotope compositions ($\delta^{13}C_{carb}$ and $\delta^{18}O_{carb}$) of calcareous shales were determined using a Thermo Fisher Scientific carbonate-preparation device and a Gas Bench II connected to a Delta Plus XL isotope ratio mass spectrometer (IRMS) that was operated in continuous He flow mode, at the Institute of Geochemistry, Chinese Academy of Sciences, Guiyang, China. The CO_2 was extracted from carbonates with 100% phosphoric acid at 70 °C for calcite and 90 °C for dolomite. The stable C and O isotope ratios are reported in delta (δ) notation as the per mil (‰) deviation relative to the Vienna Pee Dee belemnite (V-PDB) standard. The analytical reproducibility estimated from replicate analyses of the laboratory standards, Carrara marble, and Binn dolomite, is better than ±0.05‰ for $\delta^{13}C$ and ±0.1‰ for $\delta^{18}O$.

We measured the concentration of Fe in four highly reactive iron phases (Fe_{HR}): pyrite (Fe_{Py}), carbonate (Fe_{carb}), ferric oxide (Fe_{ox}) and magnetite (Fe_{mag}), and the total iron content (Fe_T). The Fe_{Py} contents were determined using the chromous chloride technique of Canfield et al. (1986), in which the sequential extraction procedure of Poulton and Canfield (2005) was used to analyze the other highly reactive iron phases, specifically Fe_{carb}, Fe_{ox} and Fe_{mag}. All the solutions were analyzed for their respective iron contents using an atomic absorption spectrometer (AAS), with an RSD of <5% for all stages. The Fe_T contents were determined using an Olympus DP-6000 hand-held X-ray fluorescence spectroscope (HH-XRF) with a Rh tube, as described in Lenniger et al. (2014). The analytical errors for Fe_T are better than 2% (Jin et al., 2016; Lenniger et al., 2014).

The TC-TOC-TS contents were measured using a Multi EA 4000 carbon/sulfur analyzer with a high-temperature furnace and acidification module (Eltra, Germany) at the China University of Geoscience (Wuhan). Analytical errors for TC-TOC-TS were ± 0.1 wt%, based on analyses of carbonate standard, AR4007 (Alpha, USA). The TIC (total inorganic carbon) content was calculated by subtracting the TOC from the TC. Concentrations of Mn and Sr were analyzed using a Perkin-Elmer ELAN 6000 inductively-coupled plasma source mass spectrometer (ICP-MS) at the Guangzhou Institute of Geochemistry, Chinese Academy of Sciences. The analytical uncertainties for Mn and Sr were smaller than 3%.

Total Hg concentrations were determined in the Institute of Geochemistry, Chinese Academy of Sciences, using a LUMEX RA915F automatic mercury vapor analyzer, which has a detection limit of 0.5 ng g^{-1}. Mercury isotope ratios were measured using the methods described in Geng et al. (2018). About 0.2–0.5 g of sample powder was digested using 5 mL of aqua regia in a water bath (95 °C for 6 hours). Certified reference materials (NIST SRM 2711, Montana soil) were prepared for analysis after every 13 samples, and digested in the same way as the samples. The samples were analyzed using a Neptune Plus multiple collector inductively coupled plasma mass spectrometer (Thermo Electron Corp, Bremen, Germany) at the University Research Facility in Chemical and Environmental Analysis (UCEA) at the Hong Kong Polytechnic University. Mercury isotopic compositions were expressed as δ and Δ values, in units of per mil (‰) following the convention recommended by Bergquist and Blum (2007).

4. Analytical results

4.1. Morphology and in-situ $\delta^{34}S$ values of pyrite

Calcareous shales from the Dongjin section consist mainly of calcite with TIC from 2.1 wt% to 10.7 wt%, organic matter with TOC from 0.2 wt% to 3.3 wt%, pyrite with TS from 0.1 wt% to 6.0 wt%, and silicate minerals dominated by quartz and clays (Fig. 3). In calcareous shales from Interval I and Interval II, pyrite occurs as disseminations and nodular aggregates. Pyrite grains in nodular aggregates are large (50–100 μm in diameter) and have extremely large positive $\delta^{34}S_{Py}$ values, ranging from +37.6‰ to +68.1‰, with an average of +60‰ (Fig. 3b; Table S1). In Interval I, disseminated pyrite comprises 6–12 vol% euhedral grains with diameters ranging from 3 μm to 25 μm and 88–94 vol% framboids with diameters ranging from 1 μm to 25.5 μm (5 μm on average) (Figs. 3c, e, f and 4; Table S2). The $\delta^{34}S_{Py}$ values of the two pyrite varieties (not distinguished) range from +8.8‰ to +21.4‰ (ca. +15.9‰ on average) (Figs. 3c; Table S1). In Interval II, pyrite framboids represent 85–92 vol% of the pyrite and their diameters range from 1 μm to 18.6 μm with an average of 5.3 μm (Table S2). The $\delta^{34}S_{Py}$ values vary from +3.2‰ to +25.7‰ (+10.2‰ on average).

Pyrite in Interval III accounts for >5 vol% of the rock (Fig. 2), and occurs mainly as large sub-euhedral to euhedral crystals (>50 μm in diameter) and small pyrite framboids (< 5 μm) (Figs. 3 and 4; Table S2). The $\delta^{34}S_{Py}$ values of these large pyrite grains range from +13.8‰ to +31.0‰. Reliable in-situ $\delta^{34}S_{Py}$ values of pyrite framboids could not be acquired by MC-LA-ICPMS due to their small grain-sizes.

4.2. Bulk rock elemental and isotopic compositions

Calcareous shales from Interval I have TS values from 0.4 wt% to 1.7 wt%, and disseminated pyrite separates have $\delta^{34}S_{Py}$ values ranging from +5.0‰ to +21.0‰ (+14.8‰ on average) (Fig. 5a; Table S3). These shales are rich in organic matter with TOC contents from 0.6 wt% to 3.3 wt%, averaging at 1.6 wt%, and TIC contents from 1.1 wt% to 7.6 wt%, averaging at 4.1 wt% (Fig. 5a; Table S3). They have relatively constant $\delta^{13}C$ values ranging from –0.98‰ to –0.79‰, $\delta^{18}O$ values from –11.2‰ to –10.1‰ and Mn/Sr ratios from 0.38 to 2.54 (Fig. 4). Samples with TS <1 wt% and TIC >3.5 wt% have CAS contents from 66 to 155 ppm and $\delta^{34}S_{CAS}$ values from +11.9‰ to +24.6‰ (average +16.7‰). The $\Delta^{34}S$ ($\delta^{34}S_{CAS} - \delta^{34}S_{Py}$) values in these samples vary from –4.2‰ to +8.3‰ with an average of +0.8‰. The Hg content of the bulk rock in Interval I ranges from 31.3 ppb to 137 ppb, which is higher than those in the other two intervals (Table S3). The $\delta^{202}Hg$ values in this interval are relatively constant (–1.08‰ to –0.74‰), whereas the $\Delta^{199}Hg$ values increase upwards from –0.16‰ to 0.00‰. The samples have high Fe_T contents ranging from 1.6 wt% to 3.0 wt%. Their Fe_{HR}/Fe_T and Fe_{Py}/Fe_{HR} values range from 0.5 to 0.66 and from 0.28 to 0.90, respectively (Figs. 4 and 5b; Table S3).

The calcareous shales from Interval II have relatively low contents of disseminated pyrite with an average TS of 0.63 wt% and

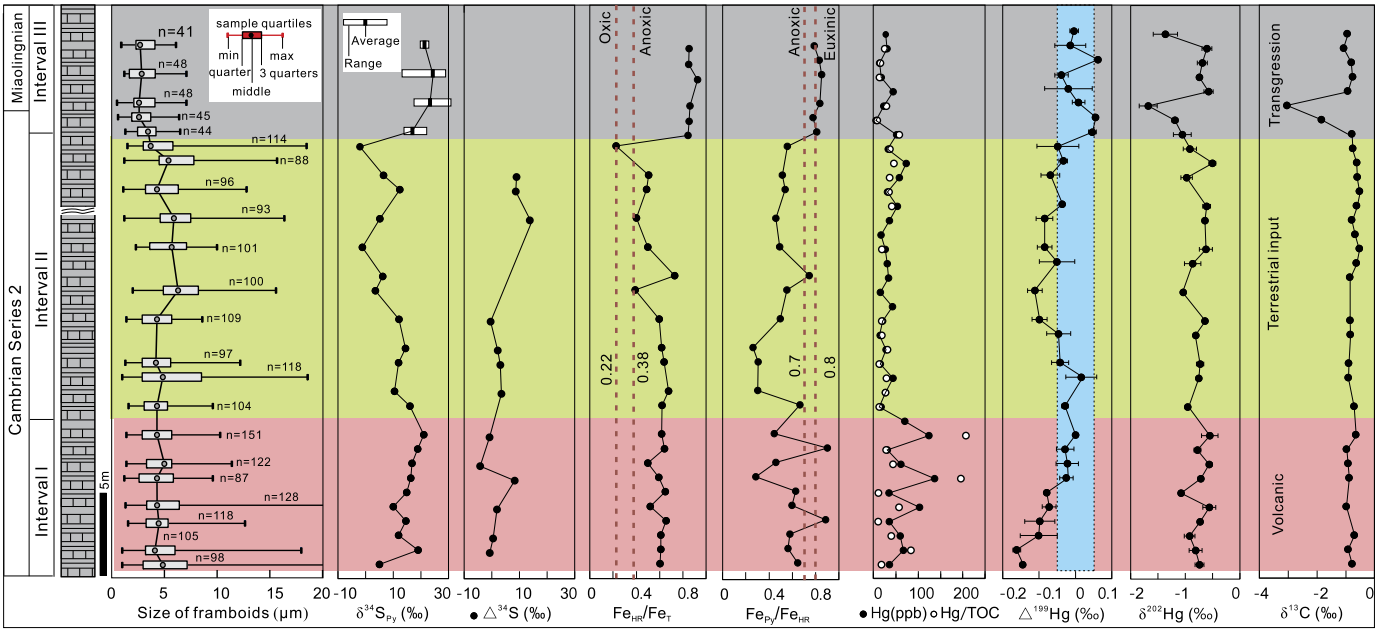

Fig. 4. A stratigraphic column showing the intervals in the CS_2-M calcareous shale succession of the Dongjin section, South China, and the variation in grain sizes of pyrite framboids, bulk-rock Hg-S-C isotopic compositions and several other compositional parameters in the three intervals.

display a gradual $\delta^{34}S_{Py}$ shift upwards from +16.1‰ to −2‰. They have a TOC content of 0.2–1.6 wt%, a TIC content of 1.2–10.3 wt%, and $\delta^{13}C$ and $\delta^{18}O$ carbonate values of −0.95 to −0.53‰ and −11.2 to −9.8‰, respectively. The CAS contents are in the range 61 to 184 ppm and their $\delta^{34}S_{CAS}$ values are +11.7‰ to +21‰ with an average of +16.1‰ (Table S3). The $\Delta^{34}S$ ($\delta^{34}S_{CAS} - \delta^{34}S_{Py}$) values increase upwards from +3 to +10‰, with an average of +5.7‰ (Table S3). The bulk rock Mn/Sr ratio ranges from 0.2 to 1.55. The Hg content of these shales is relatively constant (ca. 30 ppb), the $\Delta^{199}Hg$ values vary from slightly negative to near zero (−0.11‰ to +0.02‰) and the $\delta^{202}Hg$ values (−1.0‰ to −0.5‰) are similar to those of Interval I. The Fe_T contents ranges from 0.6 wt% to 2.8 wt% (the average is 1.90 wt%) and the Fe_{HR}/Fe_T and Fe_{py}/Fe_{HR} ratios vary from 0.25 to 0.73 (the average is 0.53) and from 0.26 to 0.75 (the average is 0.49), respectively (Figs. 4 and 5b; Table S3).

In interval III, calcareous shales have high TS contents (3.0–6.0 wt%), relatively low TOC contents (0.7–1.3 wt%), and variable Hg content (5.9–52 ppb). They have TIC contents from 2.8 wt% to 4.8 wt%, Mn/Sr ratios from 0.3 to 1.4, and constant $\delta^{18}O$ carbonate values (−11.6‰ to −10.1‰). In the basal part of this interval, the $\delta^{13}C$ values of the shales decrease sharply from −0.80‰ to −3.05‰ (Fig. 4) and are coupled to a negative shift in $\delta^{202}Hg$ from −1.05‰ to −1.68‰. The $\Delta^{199}Hg$ values range from −0.07‰ to +0.06‰, indicating the absence of mass-independent fractionation (Table S3). The Fe_T contents, Fe_{HR}/Fe_T ratios, and Fe_{py}/Fe_{HR} ratios are all high, ranging from 3.35 wt% to 4.38 wt%, from 0.82 to 0.93, and from 0.78 to 0.85, respectively (Figs. 4 and 5b; Table S3).

5. Discussion

5.1. The redox states and sulfate content of the ocean at the CS_2-M transition

5.1.1. The anoxic state and low sulfate content of the Dongjin section during Interval I

The iron speciation method, which determines the nature of 'highly-reactive' iron (Fe_{HR}) in fine-grained sediments, has been widely used to distinguish oxic, ferruginous, and euxinic conditions in siliciclastic rocks and in carbonate rocks with >0.5 wt% Fe_T (Clarkson et al., 2014; Poulton and Canfield, 2011). Anoxic sediments have Fe_{HR}/Fe_T ratios of >0.38 through the incorporation/precipitation of Fe_{HR} from the anoxic water column. Under anoxic and sulfidic (euxinic) conditions, Fe_{HR} is converted to Fe_{Py} through its reaction with H_2S to form pyrite, resulting in Fe_{Py}/Fe_{HR} ratios of >0.7–0.8 (Poulton and Canfield, 2011). All samples investigated in this study have Fe_T contents >0.5 wt% (Table S3). Calcareous shales from Interval I have an average Fe_{HR}/Fe_T ratio of 0.6 and the same average Fe_{Py}/Fe_{HR} ratio (0.6), which are indicative of an overall anoxic depositional environment low in H_2S that contains excess Fe (Figs. 4 and 5b; Table S3). Inadequate H_2S production under anoxic conditions could be caused by a limited supply of organic matter (reducer) or sulfate (reactant), or both (Poulton and Canfield, 2011; Wilkin and Barnes, 1996). Given that the TOC values represent preserved organic matter, the high TOC contents (ca. 1.6 wt%) in these calcareous shales preclude the possibility of limited organic matter supply, instead, suggesting a low sulfate supply and anoxic condition in the water column above the Dongjin section.

The low $\Delta^{34}S$ values (−4.2‰ to +8.3‰) of calcareous shales from Interval I place additional constraints on the end-CS_2 sulfur cycle (Table S3). Carbonate-associated sulfate (CAS) is the trace quantity of sulfate that replaces carbonate ions structurally in marine carbonate and can be used to represent the $\delta^{34}S$ value of sulfate in the water column (cf., Wotte et al., 2012a). The reduction of sulfate is promoted strongly by microbes (sulfate-reducing bacteria), which favor the lighter, more weakly bonded isotope of sulfur (^{32}S) (Kasten et al., 1998). The magnitude of $\Delta^{34}S$ ($\delta^{34}S_{CAS} - \delta^{34}S_{Py}$) values between sulfate in seawater and pyrite preserved in sedimentary rocks has been widely utilized to reconstruct ancient marine sulfate levels (e.g., Loyd et al., 2012; Gomes and Hurtgen, 2015). It has been estimated that a ca. 20–70‰ fractionation between sulfate and sulfide can be achieved in an aqueous system with a sulfate content of >0.2 mM (Canfield, 2001; Habicht et al., 2002; Sim et al., 2011), and that $\Delta^{34}S$ would be larger if the recycling of sulfur species, e.g., re-oxidation and disproportionation, in the water column were considered (Fike et al., 2015). This fractionation, however, is suppressed at a low sulfate content, approaching 0‰ at sulfate levels below 0.2 mM (Bradley et al., 2016; Habicht et al., 2002), because that the size of the sulfate reservoir

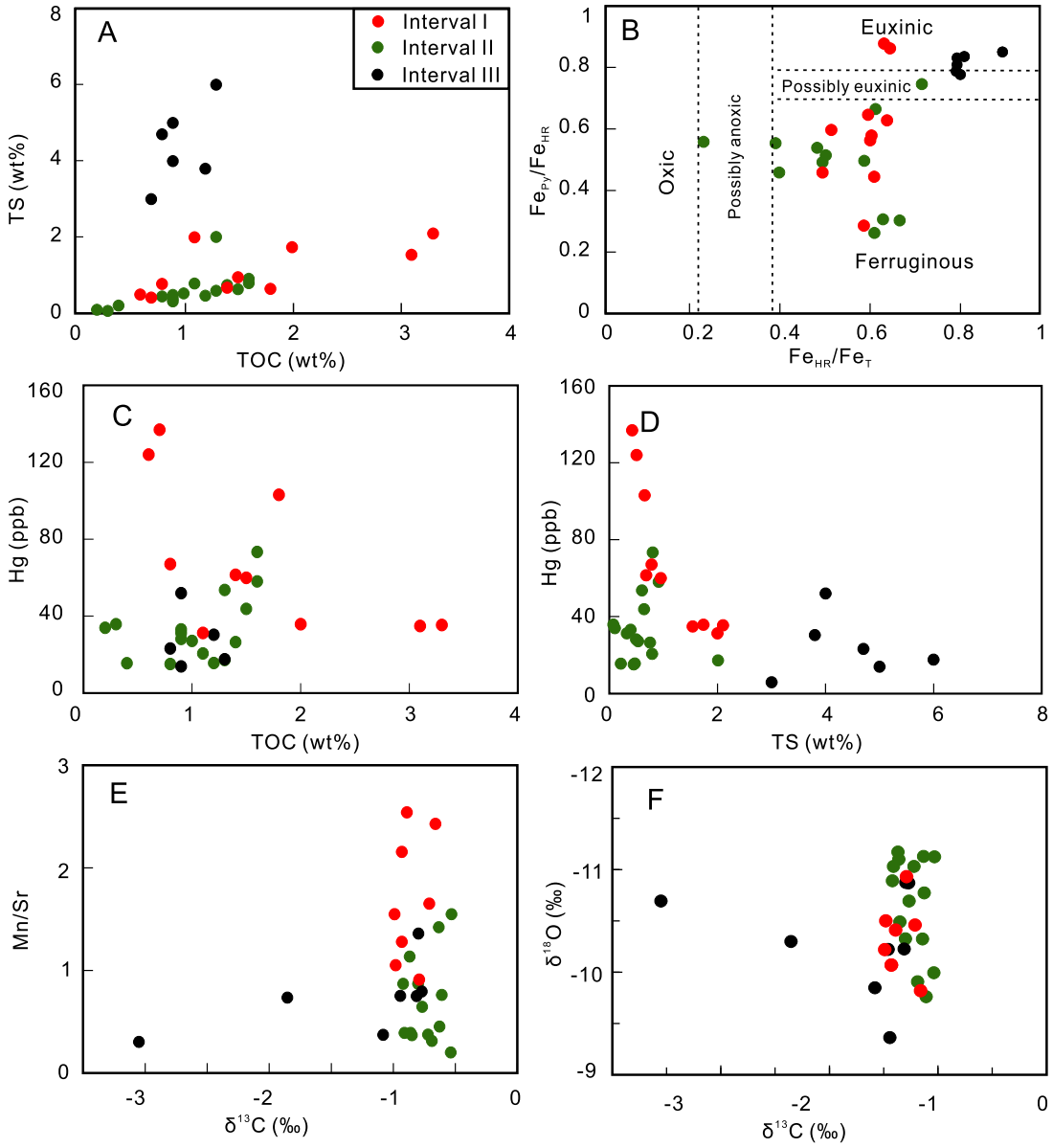

Fig. 5. Plots of TS vs. TOC (A); Fe_{Py}/Fe_{HR} vs. Fe_{HR}/Fe_T (B); Hg vs. TOC (C); Hg vs. TS (D); Mn/Sr vs. $\delta^{13}C$ (E) and, $\delta^{13}C$ vs. $\delta^{18}O$ (F) in CS_2-M strata of the Dongjin section, South China.

is sufficiently small that Rayleigh fractionation affects the S isotope equilibrium.

In Interval I, separates of disseminated pyrite grains from the calcareous shales have $\delta^{34}S_{py}$ values from +5.0‰ to +21.0‰ (+14.8‰ on average), consistent with *in-situ* analyses of individual disseminated pyrite grains, which yielded an average $\delta^{34}S_{Py}$ value of +15.9‰ (Table S1). The proportion of CAS extracted from these calcareous shales is low and has $\delta^{34}S_{CAS}$ values varying from +11.9‰ to +24.6‰. Values of $\delta^{34}S_{CAS}$ can be modified by the oxidation of pyrite during sample preparation. In the present study, this contamination was minimized by avoiding the usage of oxidants, and rapidly dissolving the carbonate slurry without drying during the extraction (Wotte et al., 2012a). To further minimize this effect on the $\delta^{34}S_{CAS}$ values, only samples with >3.5 wt% TIC and <1 wt% TS were considered further (Li et al., 2017), and these returned a very low standard deviation (<1.4‰) for duplicate analyses (Table S3) (see Supplementary Note 2 for a more detailed discussion of the reliability of the $\delta^{34}S_{CAS}$ data). The $\Delta^{34}S$ values in our samples from Interval I are in the range from –4.2‰ to +8.4‰, which is low and indicative of a sulfate-depleted end-CS_2 ocean (Fig. 4). Low $\Delta^{34}S$ values are also preserved in marine sediments deposited in end-CS_2 marginal basins elsewhere, for example, from –22.9‰ to –0.2‰ in the Carro Rajon section, Mexico (Loyd et al., 2012) and from –0.7‰ to +15.2‰ in the Cre´menes section, Spain (Wotte et al., 2012b). The results of these studies support our interpretation that the SO_4^{2-} concentration was very low in the end-CS_2 ocean (i.e., <2.0 mM; Loyd et al., 2012)).

5.1.2. *A less anoxic depositional environment with increased seawater SO_4^{2-} in Interval II*

Calcareous shales from Interval II have Fe_T contents varying from 0.6 wt% to 2.8 wt%. There is an obvious upwards decrease in Fe_{HR}/Fe_T ratios from 0.73 to 0.25 without obvious stratigraphic variation in the Fe_{Py}/Fe_{HR} ratios of the calcareous shales from Interval II (Fig. 4). The Fe speciation and TS data, therefore, suggest a decline of Fe_{HR} availability and a less anoxic depositional environment towards the late-Interval II in the Dongjin section.

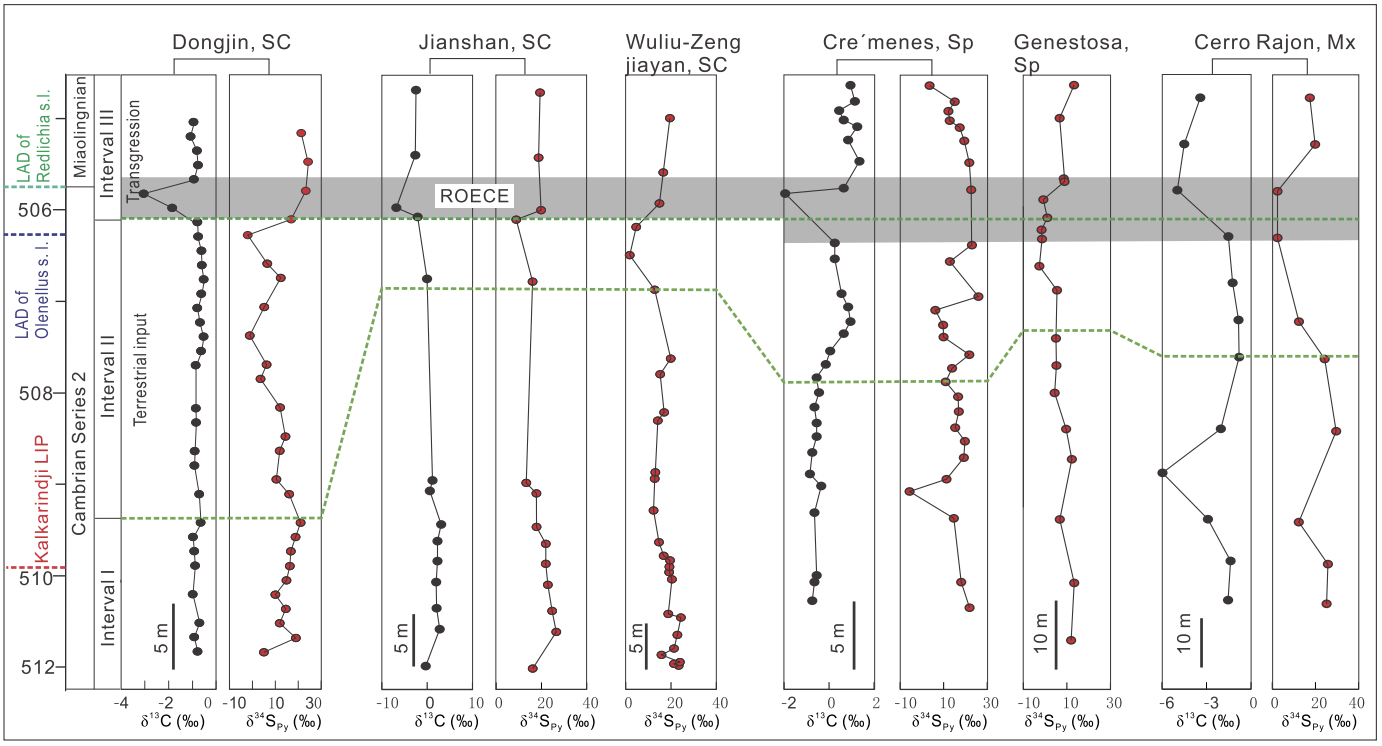

Fig. 6. A stratigraphic column showing the $\delta^{13}C$ and $\delta^{34}S_{Py}$ values in the CS_2-M sedimentary successions of the Dongjin Section, South China (SC) (this study), Jianshan and Wuliu-Zengjiayan sections, SC (Guo et al., 2014), Genestosa and Cre´menes sections, Spain (Sp) (Wotte et al., 2012b) and Carro Rajon section, Mexico (Mx) (Loyd et al., 2012).

The disseminated pyrites in calcareous shales from Interval II have $\delta^{34}S_{Py}$ values that decrease upwards stratigraphically from +16.1‰ to −2‰ (Fig. 4). This negative excursion of $\delta^{34}S_{Py}$ values at the end-CS_2 has been widely observed in the Wuliu-Zengjiayan and Jianshan sections, South China, in the Carro Rajon section, Mexico (Loyd et al., 2012), and the Genestosa and Cre´menes sections, Spain (Wotte et al., 2012b) (Fig. 6). In concert with the stratigraphically upward decreasing trend of $\delta^{34}S_{Py}$ values, $\Delta^{34}S$ values from Interval III of the Dongjin section increase upwards from +3 to +10‰ (Table S3), indicating an increase in seawater sulfate content (Loyd et al., 2012; Gomes and Hurtgen, 2015). As mentioned above, the elevated sulfate content in an aqueous system would potentially increase the sulfur isotopic fractionation between pyrite and dissolved sulfate, leading to a decrease in $\delta^{34}S_{Py}$ (Gomes and Hurtgen, 2015). The covariation of $\delta^{34}S_{Py}$ and $\Delta^{34}S$ values in calcareous shales from the Dongjin section, therefore, indicated that this globally detectable negative excursion of $\delta^{34}S_{Py}$ values was most likely due to an increase in seawater sulfate content at the end-CS_2.

5.1.3. The sudden development of euxinic conditions during Interval III

Pyrite framboids can persist for a long time, and their size distributions have been widely used in determining whether the pyrites were deposited under euxinic or non-euxinic conditions (Wignall and Newton, 1998). It has been observed that framboids crystallized directly from H_2S-rich seawater (euxinic conditions) generally have a narrow size range with an average diameter <5 μm (Wignall and Newton, 1998). This is due to the rapid crystallization of pyrite above the sediment-water interface and limited access to H_2S and/or Fe^{2+} after burial (Wignall and Newton, 1998). In H_2S-poor seawater (oxic-anoxic), conditions favorable for the crystallization of pyrite framboids are restricted to those of pore water in sediments. Because of a variation in the time-integrated availability of Fe and S, pyrite framboids formed in pore water tend to be larger and more variable in size (Wignall and Newton, 1998; Wilkin and Barnes, 1996). In calcareous shales from Interval I and Interval II, the pyrite framboids display a large size-range, i.e., from 1 μm to 25.5 μm in diameter, indicating that these grains did not precipitate in euxinic seawater. The disseminated pyrite framboids in calcareous shales from Interval III have diameters from 0.5 to 7.1 μm and a mean-diameter of ca. 3.2 μm, i.e., they are similar in size to pyrite framboids forming from euxinic seawaters in the modern Black Sea (Wignall and Newton, 1998). The small grain-size and narrow size-range of pyrite framboids in shales from Interval III, therefore reflected a rapid change in the depositional environment from an anoxic to an euxinic state.

Calcareous shales from Interval III contain abundant large-size pyrites with TS content exceeding 3.0 wt% (Fig. 4). Large pyrite grains are generally thought to precipitate and crystallize slowly from pore waters with or without frequent S-exchange with the bottom water (e.g., Cui et al., 2018). In pore waters for which there is limited S exchange with seawater, continual removal of isotopically light ^{32}S generated by BSR would lead to an increase in $\delta^{34}S$ values during the downwards diffusion of sulfate, through Rayleigh fractionation distillation (Ries et al., 2009). Pyrite precipitated under such conditions usually has much higher $\delta^{34}S_{Py}$ values than disseminated pyrite (Jørgensen and Kasten, 2006). This is exemplified by the super-heavy (isotopically) nodular pyrite from Intervals I and II, which has $\delta^{34}S_{Py}$ values of +37.6‰ to +68.1‰ (see further discussion in Supplementary Note 3). In contrast to the nodular pyrites in Intervals I and II, the large-grained pyrites in Interval III have much lower $\delta^{34}S_{Py}$ values of +13.8‰ to +31.0‰, and the values are only slightly higher than those of the disseminated pyrites (−2.0‰ to +21.0‰) (Table S3). We therefore infer that these large pyrite grains may have precipitated and grown from sulfidic pore water that was well-connected to the bottom seawater. The abundant large pyrite grains and the high TS content in calcareous shales from the Interval III are also suggestive of an euxinic depositional environment during Interval III.

In addition, the calcareous shales from the upper part of the Dongjin section also have a high Fe_{Py}/Fe_{HR} ratio of 0.78–0.85 and a high Fe_{HR}/Fe_T ratio of 0.82–0.93 (Figs. 4 and 5), features that are

typical of sediments forming under euxinic conditions. To sum up, the high pyrite content, the small grain-size of pyrite framboids, and the high Fe_{Py}/Fe_{HR} and Fe_{HR}/Fe_T ratios of the calcareous shales from this interval are indicative of the sudden onset of euxinic conditions above the Dongjin section across the CS2-M transition.

5.2. Anomalous Hg due to volcanic eruptions and a marine transgression

The Hg content and Hg isotopic composition of calcareous shales from the Dongjin section both vary stratigraphically (Fig. 4). These variations provide additional information about the changing conditions in the CS_2-M ocean that complement the C and S isotope data.

5.2.1. Volcanic eruptions revealed by Hg spikes and Hg-MIF signals

Mercury entering the ocean is readily scavenged by organic matter and transported to marine sediments (Shen et al., 2020). Anomalously high Hg concentrations and Hg/TOC ratios in marine sediments therefore provide a promising tool for identifying periods of enhanced volcanic activities (Grasby et al., 2019). Mercury concentrations in calcareous shales from Interval I in the Dongjin section are higher (70 ppb on average) than those from the other intervals in this section (34 ppb in Interval II and 27 ppb in Interval III on average). At least two distinct Hg peaks are evident for the upper part of Interval I, with the highest Hg concentration reaching 136.9 ppb (Fig. 4). The Hg concentrations do not correlate with the TOC contents, and the peak Hg values are associated with high Hg/TOC ratios (as high as 207 ppb/wt%) (Fig. 5c). Therefore, organic matter drawdown was not a driver of these Hg peaks, and the enrichments of Hg were likely a result of external Hg-loading due to extensive volcanic activity (Grasby et al., 2019). It has been reported that Hg accumulation by pyrite may also lead to anomalously high Hg concentration in sediments, e.g., in sediments deposited at the Ordovician/Silurian boundary (Shen et al., 2019). The Hg content, however, does not correlate with the TS content, and the peak Hg values are associated with high Hg/TS ratios (as high as 325 ppb/wt%) (Fig. 5d and Table S3), indicating that these enrichments of Hg were not from incorporation of Hg by sulfides (Shen et al., 2020).

Evidence of extensive volcanic activities in the upper part of Interval I is also provided by the Hg-MIF signatures. Volcanic emissions are the primary source of Hg for the environment. The volcanic Hg has been shown minor Hg-MIF with a small range of Δ^{199}Hg (–0.05‰ to +0.06‰), which may be attributed to magmatic degassing of Hg (0) (Moynier et al., 2020). Photochemical processes alter the MIF signals during global transportation of Hg, resulting in the negative Δ^{199}Hg of the atmospheric Hg (0) pool and the positive Δ^{199}Hg of the residual atmospheric Hg (II) pool (Blum et al., 2014). Oceans receive Hg mainly through atmospheric Hg (II) deposition, whereas soil and vegetation mainly receive Hg from atmospheric Hg (0) deposition. For this reason, seawater and marine sediments are characterized by positive Δ^{199}Hg, and the terrestrial inputs by negative Δ^{199}Hg (Meng et al., 2019; Yin et al., 2015). Prior to the evolution of plants, the terrestrial Hg reservoir was probably smaller and characterized by a slightly negative Δ^{199}Hg value (Fan et al., 2020), although the actual Δ^{199}Hg value of this reservoir is not well constrained. Previous studies have shown that sediments near estuaries with a high portion of continental Hg have much lower Δ^{199}Hg values (–0.15‰ to +0.16‰) than those in the deep ocean (+0.21‰ to +0.45‰) (Yin et al., 2015). In our samples, the Δ^{199}Hg/Δ^{201}Hg ratio is close to unity (see Supplementary Figure S2) and is consistent with that observed during aqueous Hg (II) photoreduction. The negative Δ^{199}Hg values of calcareous shales from Interval I indicate that the Dongjin section had a terrestrial-dominant Hg source, which is consistent with a paleo-geographical reconstruction showing that the Dongjin section was located in a continental margin basin (Fig. 1). A gradual increase of Δ^{199}Hg values from –0.16‰ at the base of Interval I to 0‰ at the top of this interval suggests an increase of volcanic Hg input, given that volcanic Hg generally has a near-zero Δ^{199}Hg value (Moynier et al., 2020; Zambardi et al., 2009). A decrease in terrestrial Hg-input might also explain the upwards increase of Δ^{199}Hg values in shales from Interval I, but it cannot explain the Hg and Hg/TOC spikes in the upper part of this interval (Fig. 4).

Spikes in the concentration of Hg before the CS_2-M transition have been reported from the Emigrant Pass, Oak Springs Summit, and Ruin Wash sections, in the western Great Basin (USA) (Faggetter et al., 2019). These Hg anomalies in the USA and South China (this study) developed synchronously with the ca. 510 Ma flood basalt volcanism of the Kalkarindji province in Australia (Faggetter et al., 2019; Hough et al., 2006; Jourdan et al., 2014), indicating that there were large inputs of volcanic Hg into the regions of Laurentia and the South China Craton.

5.2.2. Enhanced SO_4^{2-} flux into the end-CS_2 ocean in the aftermath of a LIP

Throughout Earth's history, volcanic eruptions of LIPs have led to an increase in atmospheric CO_2 and erosion of the continents, resulting in higher terrestrial input into the ocean that may have affected the ocean redox state and biogeochemical circulation (Grasby et al., 2017; Them et al., 2019). In calcareous shales from Interval II, there is a gradual decrease of Δ^{199}Hg values from +0.02‰ at the base to –0.11‰ at the top. Volcanic emissions, as noted above, are characterized by a Δ^{199}Hg value of ca. 0‰, whereas terrestrial Hg is marked by negative Δ^{199}Hg values. The negative shift of Δ^{199}Hg values, therefore, indicates that terrestrial Hg flux into the ocean outperformed the volcanic Hg input from the atmosphere. A sharp decrease in sea-level with a larger area of the continental crust exposed and eroded might cause an enhanced terrestrial Hg input into the ocean. There are, however, no obvious lithological differences between Intervals I and II in the Dongjin section and its equivalent strata in the Wuliu-Zengjiayan section and the Jianshan section, South China (Guo et al., 2014), which argue against a major ocean regression before the ROECE event.

As mentioned earlier, the decreased $\delta^{34}S_{Py}$ values reflect an increased seawater SO_4^{2-} content during Interval II, but the driving force for this variation is unclear. Enhanced terrestrial SO_4^{2-} input from continental weathering and eruptions in the aftermath of the 510 Ma Kalkarindji LIP would be a possible cause for the increased SO_4^{2-} content of the end-CS_2 oceans. Moreover, the small increase in δ^{13}C from –0.9‰ to –0.6‰ and a corresponding decrease of Δ^{199}Hg values recorded in calcareous shales from Interval II are consistent with an increase of ocean productivity and net organic burial during an enhanced terrestrial nutrient input.

5.2.3. Upwelling of deep H_2S-rich seawater at the CS_2-M transition

The abrupt increase in pyrite abundances across the boundary between Interval II and Interval III was accompanied by a negative excursion of δ^{13}C and δ^{202}Hg values and a slightly positive shift in Δ^{199}Hg values (Fig. 4). Empirical research suggests that carbonates with Mn/Sr< 10 generally retain a primary marine C isotopic signature (Kaufman et al., 1993). In samples from Interval III, Mn/Sr ratios are < 1.5, and there is no obvious correlation among δ^{13}C, δ^{18}O, and Mn/Sr values (Figs. 5e, f), indicating that the temporal variation of δ^{13}C might have been preserved and the negative δ^{13}C values in the calcareous shales were not a result of diagenesis (Li et al., 2013). Moreover, negative excursions of δ^{13}C also have been recorded in the CS_2-M shales in the Wuliu-Zengjiayan, and Jianshan sections, Guizhou province, South China, where they are interpreted to reflect marine transgression and upwelling of ^{13}C

depleted seawater (Guo et al., 2010, 2014). The sharp sedimentological and geochemical contact between Interval II and Interval III indicates that H_2S enrichment occurred rapidly. Thus, it is possible that the H_2S enrichment in Interval III also was caused by the upwelling of deep euxinic water during the transgression. The marine transgression would have caused the coastline to move towards the continent, resulting in less Hg input from terrestrial reservoirs, which is consistent with a small positive shift of the Δ^{199}Hg values in calcareous shales from Interval III.

Mass-dependent fractionation of Hg isotopes is ubiquitous and has been used as a source tracer in many studies, particularly in cases of regular stratigraphic changes (Grasby et al., 2017). Samples from Intervals I and II have a constant δ^{202}Hg value of –0.76 ± 0.16‰, which is similar to that of volcanic ash and silicate rocks, which have a mean δ^{202}Hg value of −0.68 ± 0.45‰ (Blum et al., 2014). In Interval III, the δ^{202}Hg values decrease abruptly to –1.68‰. It has been proposed that the formation of the Hg-S bond would lead to a negative shift of –0.6‰ in the δ^{202}Hg value (Foucher et al., 2013). The decrease of δ^{202}Hg in calcareous shales from Interval III thus could be attributed to the increased abundance of pyrite. However, the δ^{202}Hg value increases upwards to ca. -1‰, and is decoupled from the consistently high TS but, instead, is coupled with δ^{13}C values in calcareous shales from Interval III (Fig. 4). This indicates that the negative excursion of δ^{202}Hg might have been caused by a marine transgression rather than the precipitation of pyrite. Microbial methylation, forming monomethyl mercury (MMHg) with low δ^{202}Hg values is one of the major processes leading to MDF of Hg in aqueous systems (Blum et al., 2014). Indeed, Yin et al. (2015) showed that marine sediments (in the deep ocean) have lower δ^{202}Hg values than coastal sediments, which implies that upwelling deep waters can carry a substantial amount of Hg from deep ocean to coastal regions.

Large pyrite grains from calcareous shale of Interval III have large positive δ^{34}S values, i.e., from +13.8‰ to +31‰ (Table S1; Fig. 3d), which may reflect inheritance from deeper euxinic seawater. In modern ocean basins that receive sufficient SO_4^{2-} input for pyrite formation, e.g., the modern Black Sea, the euxinic bottom waters generally have consistently high sulfate contents, negative $\delta^{34}S_{H2S}$ values, and stable Δ^{34}S values between δ^{34}S of sulfate from surface water and δ^{34}S of pyrite in sediments (Gomes and Hurtgen, 2015). By contrast, Δ^{34}S values in low-sulfate euxinic systems are positively correlated with sulfate concentration, leading to high $\delta^{34}S_{H2S}$ values in bottom euxinic water (Gomes and Hurtgen, 2015). The high $\delta^{34}S_{Py}$ values of large-grained pyrites in Interval III may, therefore, reflect intense sulfate reduction in basins with initially low sulfate concentrations, which would have allowed a nearly quantitative reduction of sulfate and promoted high $\delta^{34}S_{H2S}$ values in the euxinic bottom water (Gomes and Hurtgen, 2015; Magnall et al., 2016). This is consistent with our interpretation, presented above, that terrestrial SO_4^{2-} input fertilized the SO_4^{2-}-depleted Nanhua Basin of Interval II. The reduction of sulfate contributed to seawater H_2S accumulation in the deep ocean.

5.3. An integrated model and implications for the trilobite crisis

Chemo-stratigraphic variations in organic-rich calcareous shales from the Dongjin section are comparable to those in the Wuliu-Zengjiayan and Jianshan sections (Guo et al., 2010, 2014). Pyrite in CS_2-M sediments from these sections has high $\delta^{34}S_{Py}$ values but displays a negative shift in $\delta^{34}S_{Py}$ values before the negative δ^{13}C excursion (Fig. 6) (Guo et al., 2010, 2014). In the Wuliu-Zengjiayan section, the negative δ^{13}C excursion at the base of Interval III coincided with the extinction of trilobites (Fig. 6) and defines the CS_2-M boundary. These geochemical similarities of the three sections, taken in conjunction with our Hg isotopic data, allow us to propose a genetic model for the S-C-Hg biogeochemical cycles in the CS_2-M Nanhua Basin.

The early Cambrian Nanhua Basin was characterized by high productivity and widespread deposition of organic-rich shales. With continuous crystallization and burial of pyrite and a limited terrestrial supply of sediment, the seawater in the Nanhua basin was depleted in SO_4^{2-} and had high $\delta^{34}S_{Py}$ values at the end of CS_2. Without sufficient SO_4^{2-} for oxidation of the organic matter (DOC and methane), the seawater in the Dongjin section became anoxic (Fig. 7a). The source of Hg in the calcareous shales deposited in the Dongjin section was mainly from continental erosion as shown by Δ^{199}Hg < 0‰. Eruptions of flood basalts in the Kalkarindji LIP at ca. 510 Ma interfered with the Hg cycle of the Earth's surface system and caused an increase of Δ^{199}Hg to a near-zero value (Fig. 7a). The volcanic eruptions increased the erosion rate of the continental crust, resulting in higher terrestrial Hg and SO_4^{2-} input into the ocean. Consequently, the Δ^{199}Hg and $\delta^{34}S_{Py}$ values decreased in Interval II (Fig. 7b). This higher terrestrial SO_4^{2-} input led to a H_2S rich reservoir in the deeper ocean. Owing to the initially low sulfate content of the CS_2 Nanhua Basin, H_2S in the deep euxinic water had high $\delta^{34}S_{Py}$ values (Fig. 7b). This euxinic water upwelled into the shallow ocean during the earliest Miaolingian, leading to abundant deposition of pyrite in carbonate muds of Interval III and mass extinction of trilobites on the shelf (as in the Wuliu-Zengjianyan section) (Fig. 7c).

Geochemical changes in the Nanhua Basin were echoed globally as discussed above, in which high δ^{34}S values of sulfate-bearing minerals and pyrite from CS_2-M sediments in Spain (Wotte et al., 2012b), Siberia (Kampschulte and Strauss, 2004) and Australia (Hough et al., 2006) have been used to propose the depletion of sulfate in the CS_2-M ocean. Moreover, the ca. 510 Ma eruptions of the Kalkarindji LIP have been shown to be recorded by the CS_2-M strata in the USA (Faggetter et al., 2019). The subsequent negative excursion of $\delta^{34}S_{Py}$ values, likewise, has been widely documented (Fig. 6) and is coincident with a positive shift of seawater $^{87}Sr/^{86}Sr$ ratios around the CS_2-M transition (Zhang et al., 2020), which also supports an increased terrestrial input after the Kalkarindji LIP. Finally, the δ^{13}C negative excursion at ca. 506 Ma (Fig. 6) was globally detectable (the ROECE event), and is considered to have been caused by a marine transgression (Guo et al., 2014; Karlstrom et al., 2020; Lin et al., 2019; Sundberg et al., 2020). Therefore, our analysis of ocean redox conditions and sulfate content suggests that changes in seawater chemistry may have been linked to a global bio-evolutionary change after the ca. 510 Ma Kalkarindji LIP. Additionally, our interpretation that upwelling of anoxic/euxinic deep seawater was the direct cause for the extinction of Redlichiid and Olebellid could explain the ca. 4 Mys time interval from the Kalkarindji LIP to the trilobite crisis.

6. Conclusions

The CS_2-M ocean was characterized by low sulfate content, resulting in high $\delta^{34}S_{Py}$ values in the sediments. Spikes in Hg content and Hg isotopic anomalies in calcareous shales from Interval I of the Dongjin section were due to volcanic Hg loading from the flood basalt eruptions of the ca. 510 Ma Kalkarindji LIP. These extensive volcanic eruptions changed the Earth's surface environment and led to higher rates of continental erosion and hence larger inputs of terrestrial material into the end-CS_2 ocean. With greater Hg and SO_4^{2-} input, the Δ^{199}Hg values of Interval II decreased, as did the $\delta^{34}S_{Py}$ values of the disseminated pyrite. Hydrogen sulfides with high δ^{34}S values were accumulated in the deep water and upwelled into the shallow ocean during a marine transgression at the CS_2-M boundary. This upwelling of deep euxinic water triggered the accumulation of pyrite and a negative excursion of δ^{13}C

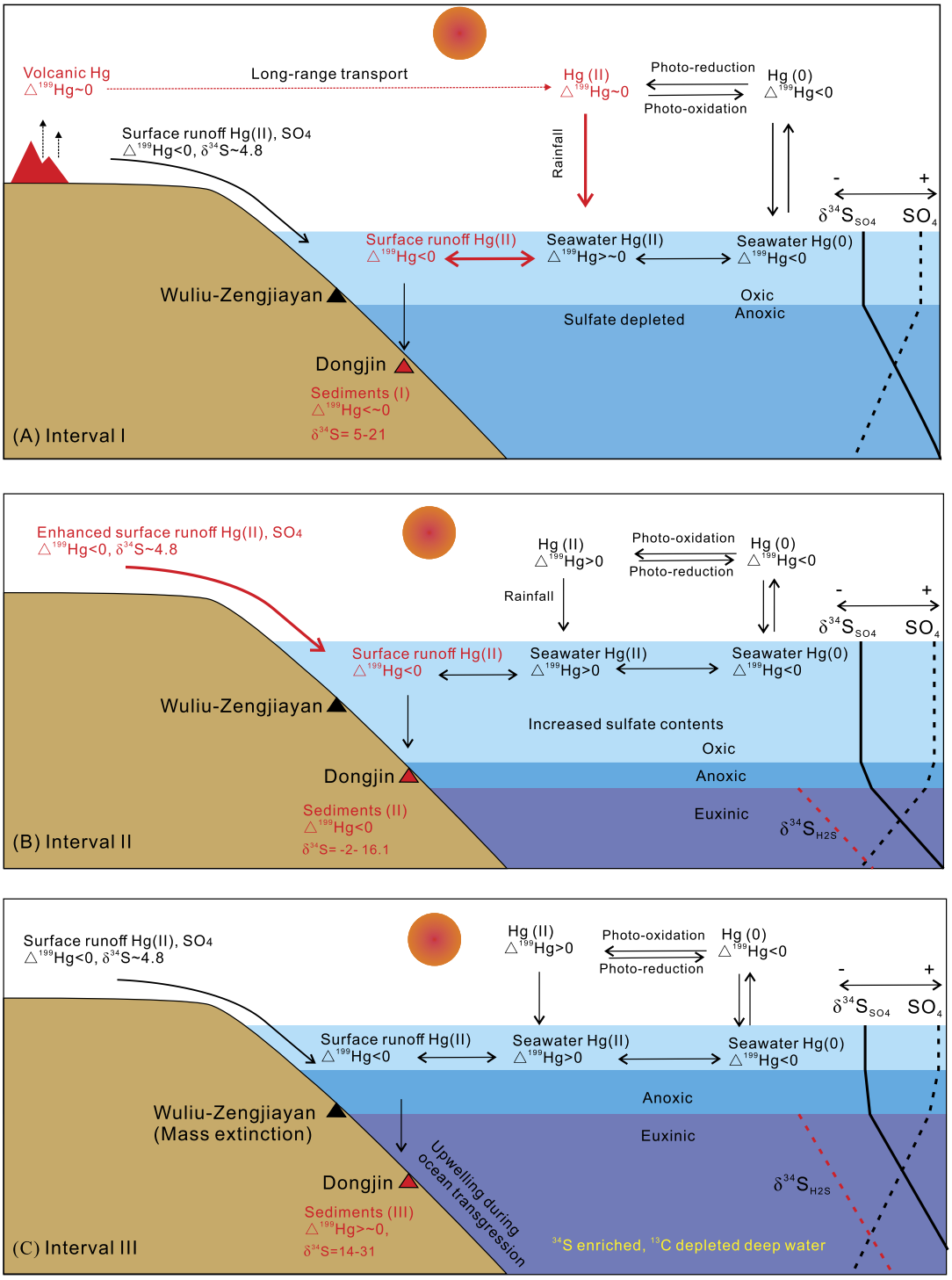

Fig. 7. A proposed model showing the evolution of the CS_2-M ocean in the Nanhua Basin, South China, and the locations of the Wuliu-Zengjiayan and Dongjin sections during this evolution. The unit for the Hg and S isotopic data in the figure is '‰'.

values in calcareous shales from Interval III and was likely responsible for the extinction of Redlichiid and Olebellid.

CRediT authorship contribution statement

Ze-Rui Ray Liu: Conceptualization, Investigation, Methodology, Writing – original draft, Writing – review & editing. **Mei-Fu Zhou:** Conceptualization, Investigation, Project administration, Supervision, Writing – original draft. **Wei Terry Chen:** Investigation, Methodology. **Anthony E. Williams-Jones:** Writing – original draft, Writing – review & editing. **Xiang-Dong Li:** Methodology. **Run-Sheng Yin:** Conceptualization, Methodology, Writing – original draft. **Hugh O'Brien:** Methodology. **Yann Lahaye:** Methodology.

Declaration of competing interest

The authors declare that they have no known competing financial interests or personal relationships that could have appeared to influence the work reported in this paper.

Acknowledgements

This research was financially supported by the National Natural Science Foundation of China (41772087). We thank Dr. Wen Zhao for his assistance in the field, Dr. Zihu Zhang for the S isotope analysis, Prof. Xinbin Feng, Dr. Wenjun Hu and Dr. Hongyan Geng for the Hg analysis, and Prof. Chao Li for his discussion and suggestions during the revision. We gratefully acknowledge the support of the University Research Facility in Chemical and Environmental Analysis (UCEA), the Hong Kong Polytechnic University. Prof. Frédéric Moynier is thanked for efficient editorial handling. The constructive comments from Prof. Ganqing Jiang and Dr. Geoff Gilleaudeau that helped improve the paper significantly are much appreciated.

Appendix A. Supplementary material

Supplementary material related to this article can be found online at https://doi.org/10.1016/j.epsl.2021.116947.

References

Bergquist, B.A., Blum, J.D., 2007. Mass-dependent and-independent fractionation of Hg isotopes by photoreduction in aquatic systems. Science 318, 417–420. https://doi.org/10.1126/science.1148050.

Blum, J.D., Sherman, L.S., Johnson, M.W., 2014. Mercury isotopes in Earth and environmental sciences. Annu. Rev. Earth Planet. Sci. 42, 249–269. https://doi.org/10.1146/annurev-earth-050212-124107.

Bradley, A.S., Leavitt, W.D., Schmidt, M., Knoll, A.H., Girguis, P.R., Johnston, D.T., 2016. Patterns of sulfur isotope fractionation during microbial sulfate reduction. Geobiology 14, 91–101. https://doi.org/10.1111/gbi.12149.

Canfield, D.E., 2001. Biogeochemistry of sulfur isotopes. Rev. Mineral. Geochem. 43, 607–636. https://doi.org/10.2138/gsrmg.43.1.607.

Canfield, D.E., Farquhar, J., 2009. Animal evolution, bioturbation, and the sulfate concentration of the oceans. Proc. Natl. Acad. Sci. USA 106, 8123–8127. https://doi.org/10.1073/pnas.0902037106.

Canfield, D.E., Raiswell, R., Westrich, J.T., Reaves, C.M., Berner, R.A., 1986. The use of chromium reduction in the analysis of reduced inorganic sulfur in sediments and shales. Chem. Geol. 54, 149–155. https://doi.org/10.1016/0009-2541(86)90078-1.

Chang, C., Hu, W.X., Wang, X.L., Huang, K.J., Yang, A.H., Zhang, X.L., 2019. Nitrogen isotope evidence for an oligotrophic shallow ocean during the Cambrian Stage 4. Geochim. Cosmochim. Acta 257, 49–67. https://doi.org/10.1016/j.gca.2019.04.021.

Clarkson, M.O., Poulton, S.W., Guilbaud, R., Wood, R.A., 2014. Assessing the utility of Fe/Al and Fe-speciation to record water column redox conditions in carbonate-rich sediments. Chem. Geol. 382, 111–122. https://doi.org/10.1016/j.chemgeo.2014.05.031.

Cui, H., Kitajima, K., Spicuzza, M.J., Fournelle, J.H., Denny, A., Ishida, A., Zhang, F.F., Valley, J.W., 2018. Questioning the biogenicity of Neoproterozoic superheavy pyrite by SIMS. Am. Mineral. 103, 1362–1400. https://doi.org/10.2138/am-2018-6489.

Darroch, S.A.F., Smith, E.F., Laflamme, M., Erwin, D.H., 2018. Ediacaran extinction and Cambrian explosion. Trends Ecol. Evol. 33, 653–663. https://doi.org/10.1016/j.tree.2018.06.003.

Faggetter, L.E., Wignall, P.B., Pruss, S.B., Jones, D.S., Grasby, S., Widdowson, M., Newton, R.J., 2019. Mercury chemostratigraphy across the Cambrian Series 2-Series 3 boundary: evidence for increased volcanic activity coincident with extinction? Chem. Geol. 510, 188–199. https://doi.org/10.1016/j.chemgeo.2019.02.006.

Fan, H., Fu, X., Ward, J.F., Yin, R., Wen, H., Feng, X., 2020. Mercury isotopes track the cause of carbon perturbations in the Ediacaran ocean. Geology 49. https://doi.org/10.1130/G48266.1.

Fike, D.A., Bradley, A.S., Rose, C.V., 2015. Rethinking the ancient sulfur cycle. Annu. Rev. Earth Planet. Sci. 43, 593–622. https://doi.org/10.1146/annurev-earth-060313-054802.

Foucher, D., Hintelmann, H., Al, T.A., MacQuarrie, K.T., 2013. Mercury isotope fractionation in waters and sediments of the Murray Brook mine watershed (New Brunswick, Canada): tracing mercury contamination and transformation. Chem. Geol. 336, 87–95. https://doi.org/10.1016/j.chemgeo.2012.04.014.

Geng, H.Y., Yin, R.S., Li, X.D., 2018. An optimized protocol for high precision measurement of Hg isotopic compositions in samples with low concentrations of Hg using MC-ICP-MS. J. Anal. At. Spectrom. 33, 1932–1940. https://doi.org/10.1039/c8ja00255j.

Gomes, M.L., Hurtgen, M.T., 2015. Sulfur isotope fractionation in modern euxinic systems: implications for paleoenvironmental reconstructions of paired sulfate-sulfide isotope records. Geochim. Cosmochim. Acta 157, 39–55. https://doi.org/10.1016/j.gca.2015.02.031.

Grasby, S.E., Shen, W.J., Yin, R.S., Gleason, J.D., Blum, J.D., Lepak, R.F., Hurley, J.P., Beauchamp, B., 2017. Isotopic signatures of mercury contamination in latest Permian oceans. Geology 45, 55–58. https://doi.org/10.1130/G38487.1.

Grasby, S.E., Them II, T.R., Chen, Z., Yin, R., Ardakani, O.H., 2019. Mercury as a proxy for volcanic emissions in the geologic record. Earth-Sci. Rev. 196, 102880. https://doi.org/10.1016/j.earscirev.2019.102880.

Guo, Q., Strauss, H., Liu, C., Zhao, Y., Yang, X., Peng, J., Yang, H., 2010. A negative carbon isotope excursion defines the boundary from Cambrian Series 2 to Cambrian Series 3 on the Yangtze Platform, South China. Palaeogeogr. Palaeoclimatol. Palaeoecol. 285, 143–151. https://doi.org/10.1016/j.palaeo.2009.11.005.

Guo, Q.J., Strauss, H., Zhao, Y.L., Yang, X.L., Peng, J., Yang, Y.N., Deng, Y.A., 2014. Reconstructing marine redox conditions for the transition between Cambrian Series 2 and Cambrian Series 3, Kaili area, Yangtze Platform: evidence from biogenic sulfur and degree of pyritization. Palaeogeogr. Palaeoclimatol. Palaeoecol. 398, 144–153. https://doi.org/10.1016/j.palaeo.2013.10.003.

Habicht, K.S., Gade, M., Thamdrup, B., Berg, P., Canfield, D.E., 2002. Calibration of sulfate levels in the Archean Ocean. Science 298, 2372–2374. https://doi.org/10.1126/science.1078265.

Hough, M.L., Shields, G.A., Evins, L.Z., Strauss, H., Henderson, R.A., Mackenzie, S., 2006. A major sulphur isotope event at c. 510 Ma: a possible anoxia-extinction-volcanism connection during the Early-Middle Cambrian transition? Terra Nova 18, 257–263. https://doi.org/10.1111/j.1365-3121.2006.00687.x.

Hughes, N.C., 2016. The Cambrian palaeontological record of the Indian subcontinent. Earth-Sci. Rev. 159, 428–461. https://doi.org/10.1016/j.earscirev.2016.06.004.

Jin, C.S., Li, C., Algeo, T.J., Planaysky, N.J., Cui, H., Yang, X.L., Zhao, Y.L., Zhang, X.L., Xie, S.C., 2016. A highly redox-heterogeneous ocean in South China during the early Cambrian (~ 529-514 Ma): implications for biota-environment co-evolution. Earth Planet. Sci. Lett. 441, 38–51. https://doi.org/10.1016/j.epsl.2016.02.019.

Jørgensen, B.B., Kasten, S., 2006. Sulfur cycling and methane oxidation. In: Marine Geochemistry. Springer, pp. 271–309.

Jourdan, F., Hodges, K., Sell, B., Schaltegger, U., Wingate, M.T.D., Evins, L.Z., Blenkinsop, T., 2014. High-precision dating of the Kalkarindji large igneous province, Australia, and synchrony with the Early–Middle Cambrian (Stage 4–5) extinction. Geology 42, 543–546. https://doi.org/10.1130/G35434.1.

Ju, T.Y., 1989. Subdivision and correlation of the Cambrian system in Zhejiang province. Geol. Zhejiang 5, 1–15 (in Chinese with English abstract).

Kampschulte, A., Strauss, H., 2004. The sulfur isotopic evolution of Phanerozoic seawater based on the analysis of structurally substituted sulfate in carbonates. Chem. Geol. 204, 255–286. https://doi.org/10.1016/j.chemgeo.2003.11.013.

Karlstrom, K.E., Mohr, M.T., Schmitz, M.D., Sundberg, F.A., Rowland, S.M., Blakey, R., Foster, J.R., Crossey, L.J., Dehler, C.M., Hagadorn, J.W., 2020. Redefining the Tonto Group of Grand Canyon and recalibrating the Cambrian time scale. Geology 48, 425–430. https://doi.org/10.1130/G46755.1.

Kasten, S., Freudenthal, T., Gingele, F.X., Schulz, H.D., 1998. Simultaneous formation of iron-rich layers at different redox boundaries in sediments of the Amazon deep-sea fan. Geochim. Cosmochim. Acta 62, 2253–2264. https://doi.org/10.1016/S0016-7037(98)00093-3.

Kaufman, A.J., Jacobsen, S.B., Knoll, A.H., 1993. The Vendian record of Sr and C isotopic variations in seawater: implications for tectonics and paleoclimate. Earth Planet. Sci. Lett. 120, 409–430. https://doi.org/10.1016/0012-821X(93)90254-7.

Lenniger, M., Nøhr-Hansen, H., Hills, L.V., Bjerrum, C.J., 2014. Arctic black shale formation during Cretaceous oceanic anoxic event 2. Geology 42, 799–802. https://doi.org/10.1130/G35732.1.

Li, C., Hardisty, D.S., Luo, G., Huang, J., Algeo, T.J., Cheng, M., Shi, W., An, Z.H., Tong, J., Xie, S.C., Jiao, N., Lyons, T.W., 2017. Uncovering the spatial heterogeneity of Ediacaran carbon cycling. Geobiology 15, 211–224. https://doi.org/10.1111/gbi.12222.

Li, D., Ling, H.F., Shields-Zhou, G.A., Chen, X., Cremonese, L., Och, L., Thirlwall, M., Manning, C.J., 2013. Carbon and strontium isotope evolution of seawater across the Ediacaran-Cambrian transition: evidence from the Xiaotan section, NE Yunnan, South China. Precambrian Res. 225, 128–147. https://doi.org/10.1016/j.precamres.2012.01.002.

Lin, J.P., Sundberg, F.A., Jiang, G.Q., Montanez, I.P., Wotte, T., 2019. Chemostratigraphic correlations across the first major trilobite extinction and faunal turnovers between Laurentia and South China. Sci. Rep. 9. https://doi.org/10.1038/s41598-019-53685-2.

Liu, Z.R., Zhou, M.-F., Williams-Jones, A.E., Wang, W., Gao, J.-F., 2019. Diagenetic mobilization of Ti and formation of brookite/anatase in early Cambrian black shales, South China. Chem. Geol. 506, 79–96. https://doi.org/10.1016/j.chemgeo.2018.12.022.

Loyd, S.J., Marenco, P.J., Hagadorn, J.W., Lyons, T.W., Kaufman, A.J., Sour-Tovar, F., Corsetti, F.A., 2012. Sustained low marine sulfate concentrations from the Neoproterozoic to the Cambrian: insights from carbonates of northwestern Mexico and eastern California. Earth Planet. Sci. Lett. 339, 79–94. https://doi.org/10.1016/j.epsl.2012.05.032.

Magnall, J.M., Gleeson, S.A., Stern, R.A., Newton, R.J., Poulton, S.W., Paradis, S., 2016. Open system sulphate reduction in a diagenetic environment - Isotopic analysis of barite (δ^{34}S and δ^{18}O) and pyrite (δ^{34}S) from the Tom and Jason Late Devonian Zn-Pb-Ba deposits, Selwyn Basin, Canada. Geochim. Cosmochim. Acta 180, 146–163. https://doi.org/10.1016/j.gca.2016.02.015.

Meng, M., Sun, R.Y., Liu, H.W., Yu, B., Yin, Y.G., Hu, L.G., Shi, J.B., Jiang, G.B., 2019. An integrated model for input and migration of mercury in Chinese coastal sediments. Environ. Sci. Technol. 53, 2460–2471. https://doi.org/10.1021/acs.est.8b06329.

Moynier, F., Chen, J., Zhang, K., Cai, H., Wang, Z., Jackson, M.G., Day, J.M., 2020. Chondritic mercury isotopic composition of Earth and evidence for evaporative equilibrium degassing during the formation of eucrites. Earth Planet. Sci. Lett. 551, 116544. https://doi.org/10.1016/j.epsl.2020.116544.

Paterson, J.R., Edgecombe, G.D., Lee, M.S.Y., 2019. Trilobite evolutionary rates constrain the duration of the Cambrian explosion. Proc. Natl. Acad. Sci. USA 116, 4394–4399. https://doi.org/10.1073/pnas.1819366116.

Peng, S.C., Babcock, L.E., Zuo, J.X., Zhu, X.J., Lin, H.L., Yang, X.F., Qi, Y.P., Bagnoli, G., Wang, L.W., 2012. Global Standard Stratotype-Section and Point (GSSP) for the Base of the Jiangshanian Stage (Cambrian: Furongian) at Duibian, Jiangshan, Zhejiang, Southeast China. Episodes 35, 462–477. https://doi.org/10.18814/epiiugs/2012/v35i4/002.

Poulton, S.W., Canfield, D.E., 2005. Development of a sequential extraction procedure for iron: implications for iron partitioning in continentally derived particulates. Chem. Geol. 214, 209–221. https://doi.org/10.1016/j.chemgeo.2004.09.003.

Poulton, S.W., Canfield, D.E., 2011. Ferruginous conditions: a dominant feature of the ocean through Earth's history. Elements 7, 107–112. https://doi.org/10.2113/gselements.7.2.107.

Ries, J.B., Fike, D.A., Pratt, L.M., Lyons, T.W., Grotzinger, J.P., 2009. Superheavy pyrite ($\delta^{34}S_{pyr} > \delta^{34}S_{CAS}$) in the terminal Proterozoic Nama Group, southern Namibia: a consequence of low seawater sulfate at the dawn of animal life. Geology 37, 743–746. https://doi.org/10.1130/G25775a.1.

Shen, J., Algeo, T.J., Chen, J.B., Planavsky, N.J., Feng, Q.L., Yu, J.X., Liu, J.L., 2019. Mercury in marine Ordovician/Silurian boundary sections of South China is sulfide-hosted and non-volcanic in origin. Earth Planet. Sci. Lett. 511, 130–140. https://doi.org/10.1016/j.epsl.2019.01.028.

Shen, J., Feng, Q., Algeo, T.J., Liu, J., Zhou, C., Wei, W., Liu, J., Them II, T.R., Gill, B.C., Chen, J., 2020. Sedimentary host phases of mercury (Hg) and implications for use of Hg as a volcanic proxy. Earth Planet. Sci. Lett. 543, 116333. https://doi.org/10.1016/j.epsl.2020.116333.

Sim, M.S., Bosak, T., Ono, S., 2011. Large sulfur isotope fractionation does not require disproportionation. Science 333, 74–77. https://doi.org/10.1126/science.1205103.

Sundberg, F., Karlstrom, K., Geyer, G., Foster, J., Hagadorn, J., Mohr, M., Schmitz, M., Dehler, C., Crossey, L., 2020. Asynchronous trilobite extinctions at the early to middle Cambrian transition. Geology 48, 441–445. https://doi.org/10.1130/G46913.1.

Them, T.R., Jagoe, C.H., Caruthers, A.H., Gill, B.C., Grasby, S.E., Grocke, D.R., Yin, R., Owens, J.D., 2019. Terrestrial sources as the primary delivery mechanism of mercury to the oceans across the Toarcian Oceanic Anoxic Event (Early Jurassic). Earth Planet. Sci. Lett. 507, 62–72. https://doi.org/10.1016/j.epsl.2018.11.029.

Thibodeau, A.M., Ritterbush, K., Yager, J.A., West, A.J., Ibarra, Y., Bottjer, D.J., Berelson, W.M., Bergquist, B.A., Corsetti, F.A., 2016. Mercury anomalies and the timing of biotic recovery following the end-Triassic mass extinction. Nat. Commun. 7. https://doi.org/10.1038/Ncomms11147.

Wang, J., Li, Z.X., 2003. History of Neoproterozoic rift basins in South China: implications for Rodinia break-up. Precambrian Res. 122, 141–158. https://doi.org/10.1016/S0301-9268(02)00209-7.

Wignall, P.B., Newton, R., 1998. Pyrite framboid diameter as a measure of oxygen deficiency in ancient mudrocks. Am. J. Sci. 298, 537–552. https://doi.org/10.2475/ajs.298.7.537.

Wilkin, R.T., Barnes, H.L., 1996. Pyrite formation by reactions of iron monosulfides with dissolved inorganic and organic sulfur species. Geochim. Cosmochim. Acta 60, 4167–4179. https://doi.org/10.1016/S0016-7037(97)81466-4.

Wotte, T., Shields-Zhou, G.A., Strauss, H., 2012a. Carbonate-associated sulfate: experimental comparisons of common extraction methods and recommendations toward a standard analytical protocol. Chem. Geol. 326, 132–144. https://doi.org/10.1016/j.chemgeo.2012.07.020.

Wotte, T., Strauss, H., Fugmann, A., Garbe-Schonber, D., 2012b. Paired $\delta^{34}S$ data from carbonate-associated sulfate and chromium-reducible sulfur across the traditional Lower-Middle Cambrian boundary of W-Gondwana. Geochim. Cosmochim. Acta 85, 228–253. https://doi.org/10.1016/j.gca.2012.02.013.

Yao, W.-H., Li, Z.-X., 2016. Tectonostratigraphic history of the Ediacaran–Silurian Nanhua foreland basin in South China. Tectonophysics, 31–51. https://doi.org/10.1016/j.tecto.2016.02.012.

Yin, R.S., Feng, X.B., Chen, B.W., Zhang, J.J., Wang, W.X., Li, X.D., 2015. Identifying the sources and processes of mercury in subtropical estuarine and ocean sediments using Hg isotopic composition. Environ. Sci. Technol. 49, 1347–1355. https://doi.org/10.1021/es504070y.

Zambardi, T., Sonke, J.E., Toutain, J.P., Sortino, F., Shinohara, H., 2009. Mercury emissions and stable isotopic compositions at Vulcano Island (Italy). Earth Planet. Sci. Lett. 277, 236–243. https://doi.org/10.1016/j.epsl.2008.10.023.

Zhang, W.H., Shi, X.Y., Jiang, G.Q., Tang, D.J., Wang, X.Q., 2015. Mass-occurrence of oncoids at the Cambrian Series 2-Series 3 transition: implications for microbial resurgence following an Early Cambrian extinction. Gondwana Res. 28, 432–450. https://doi.org/10.1016/j.gr.2014.03.015.

Zhang, X.L., Liu, W., Zhao, Y.L., 2008. Cambrian Burgess Shale-type Lagerstatten in South China: distribution and significance. Gondwana Res. 14, 255–262. https://doi.org/10.1016/j.gr.2007.06.008.

Zhang, Y., Yang, T., Hohl, S.V., Zhu, B., He, T., Pan, W., Chen, Y., Yao, X., Jiang, S., 2020. Seawater carbon and strontium isotope variations through the late Ediacaran to late Cambrian in the Tarim Basin. Precambrian Res. 345, 105769. https://doi.org/10.1016/j.precamres.2020.105769.

Zhao, Y.L., Yuan, J.L., Babcock, L.E., Guo, Q.J., Peng, J., Yin, L.M., Yang, X.L., Peng, S.C., Wang, C.J., Gaines, R.R., Esteve, J., Tai, T.S., Yang, R.D., Wang, Y., Sun, H.J., Yang, Y.N., 2019. Global Standard Stratotype-Section and Point (GSSP) for the conterminous base of the Miaolingian Series and Wulivan Stage (Cambrian) at Balang, Jianhe, Guizhou, China. Episodes 42, 165–184. https://doi.org/10.18814/epiiugs/2019/019013.

Zhu, M.Y., Yang, A.H., Yuan, J.L., Li, G.X., Zhang, J.M., Zhao, F.C., Ahn, S.Y., Miao, L.Y., 2019. Cambrian integrative stratigraphy and timescale of China. Sci. China Earth Sci. 62, 25–60. https://doi.org/10.1007/s11430-017-9291-0.